ChemComm

COMMUNICATION

View Article Online
View Journal

Check for updates

Cite this: DOI: 10.1039/d5cc02703a

Received 13th May 2025,
Accepted 5th August 2025

DOI: 10.1039/d5cc02703a

rsc.li/chemcomm

Open Access Article. Published on 14 August 2025. Downloaded on 8/23/2025 4:20:50 PM.
This article is licensed under a Creative Commons Attribution 3.0 Unported Licence.

Grain-resolved mapping of oxygen evolution activation on a Ni-superalloy

Črtomir Donik,[a] Luka Suhadolnik,*[b] Blaž Tomc,[b] Anton Voronkin,[c] Jon Ustarroz,[cd] Marjan Bele,[b] Matjaž Godec[a] and Nejc Hodnik *[ab]

We report the first grain-resolved mapping of oxygen evolution reaction (OER) activation on a Ni-based superalloy using identical-location EBSD, complemented by IL-SEM, IL-EDS, and SECCM. NiFe (oxy)hydroxide film formation and OER activity are strongly influenced by grain size and orientation, with (111)-oriented and smaller grains undergoing pronounced structural, chemical, and electrochemical transformations. These findings reveal pronounced microstructure heterogeneity in OER and establish IL-EBSD as a powerful tool for the microstructure-guided design of advanced electrocatalysts.

Alkaline water electrolysis is a century-old and technologically mature process that remains one of the most scalable and cost-effective methods for green hydrogen production. Yet, despite its long industrial history, key aspects of how electrode materials evolve during initiation and operation remain poorly understood. As the energy transition accelerates, the need for efficient, durable, and flexible alkaline electrolyzers for intermittent solar and wind power grows.[1,2]

For alkaline conditions, NiFe-based (oxy)hydroxides are among the most promising catalysts for the oxygen evolution reaction (OER) due to their earth abundance, cost-effectiveness, and high catalytic activity.[3,4] Their performance depends on the Fe/Ni ratio, with optimal activity typically observed for a 0.2–0.4 ratio.[5,6] However, the precise nature of the active sites, whether Fe- and/or Ni-centered, or due to synergistic interactions and dissolution/redeposition from the electrolyte, remains under debate.[7,8] These catalytic films form *in situ* under OER conditions when applied to NiFe-containing alloys, although they can also be synthesized *via* methods such as co-precipitation or electrodeposition. However, the microstructure–activity–stability relationships, particularly under harsh OER and start-stop scenarios (*e.g.*, reverse current phenomenon), remain poorly understood.[6,9]

In this context, commercial Ni-containing alloys such as stainless steels and Inconel have emerged as promising anode candidates, offering a compelling combination of catalytic efficiency and durability.[5] Electrochemical treatment of these alloys leads to the formation of nanostructured NiFe (oxy)hydroxide surface layers, eliminating the need for additional catalyst coatings. Notably, Inconel yields one of the thickest active layers (~40 nm), which correlates with its high electrochemical capacity.[5] Due to nickel's cost and scarcity, shifting toward lower-Ni steels that still form active NiFe (oxy)hydroxide films offers a scalable, cost-effective path for alkaline OER electrodes.

Current strategies to improve OER performance primarily focus on compositional tuning, surface coatings, or nano-structuring.[10] However, these approaches frequently neglect microstructural characteristics, such as grain orientations, grain boundaries and local crystallographic heterogeneities.[11] These materials' features play a crucial role in determining mechanical properties; however, they also have electrochemical properties like corrosion resistance and electrocatalysis capabilities. Beyond grain size and orientation, microstructural features such as grain boundary density, strain, and crystallographic defects may also influence the growth and activity of NiFe (oxy)hydroxide films. While microstructure-function relationships are studied in metallurgy, these aspects remain underexplored in electrocatalysis, primarily due to the lack of utilization of spatially resolved techniques capable of tracking changes at the sub-micrometre level. A promising solution is identical location electron microscopy (IL-EM), which enables tracking of structural and compositional changes in the same regions of a material before and after electrochemical treatment. IL-EM has provided essential insight into electrocatalyst restructuring degradation mechanisms (Fig. 1).[12–14]

In this study, we present the first use of identical location electron backscatter diffraction (IL-EBSD) to investigate the grain-specific activation of electrocatalytic materials. We reveal how Inconel 625 (IN625), a commercially available Ni-based superalloy with homogeneous composition of Ni/Cr/Fe/Mo/Nb

[a] *Institute of Metals and Technology, Lepi pot 11, 1000 Ljubljana, Slovenia. E-mail: nejc.hodnik@ki.si*
[b] *National Institute of Chemistry, Hajdrihova 19, 1000 Ljubljana, Slovenia*
[c] *Chemistry of Surfaces, Interfaces and Nanomaterials (ChemSIN), Université libre de Bruxelles, 1050 Brussels, Belgium*
[d] *Research Group Electrochemical and Surface Engineering (SURF), Vrije Universiteit Brussel, Pleinlaan 2, 1050 Brussels, Belgium*

Open Access Article. Published on 14 August 2025. Downloaded on 8/23/2025 4:20:50 PM.
This article is licensed under a Creative Commons Attribution 3.0 Unported Licence.

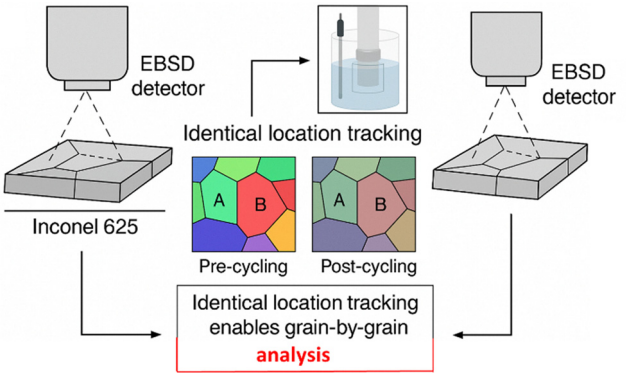

Fig. 1 Schematic showing IL-EBSD workflow, involving EBSD characterization of Inconel 625 before and after electrochemical cycling at the identical location. Comparative analysis of the EBSD images reveals structural changes induced by cycling.

(at% 62.2/23.3/6.7/5.4/2.4), changes during electrochemical cycling. We show that NiFe (oxy)hydroxide film formation depends on grain size and potentially crystallographic orientation. This represents the first direct visualization of grain-resolved structural correlations in OER electrocatalysts.

To study grain-specific NiFe (oxy)hydroxide film growth, polished IN625 was electrochemically activated under OER conditions by cycling between 1.2 and 1.6 V *vs.* RHE at 20 mV s^{-1} for 200 cycles (Fig. 2). A typical oxidation of nickel(II) hydroxide to nickel(III) oxyhydroxide peak is observed at 1.35–1.45 V *vs.* RHE followed by the onsets of OER at approximately 1.5 V *vs.* RHE, making this material a very promising OER catalyst. Further experimental information, details and results are available in the SI.

EBSD inverse pole figure (IPF-Z) maps and SEM imaging were used to analyze the polished surface of IN626 before and after cycling at identical locations. Due to its orientation-specific signal, EBSD enables direct determination of grain orientations (see the insert in Fig. 3) and grain sizes (see the distribution in Fig. S1). To resolve grain orientations beneath the oxidized surface, we applied EBSD postprocessing using spherical indexing,[16] which successfully recovered crystallographic information otherwise lost

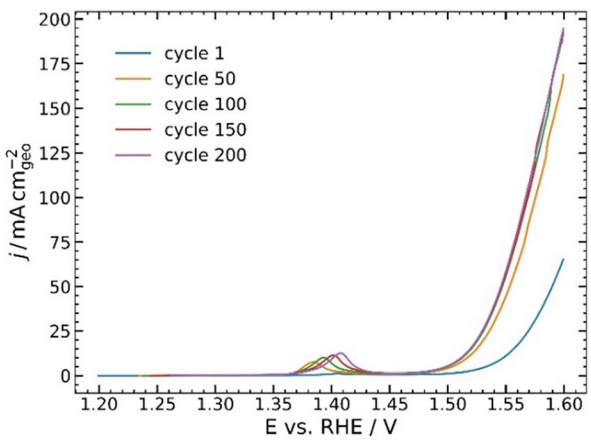

Fig. 2 Subsequent activation polarization curves of Inconel in 1 M KOH.

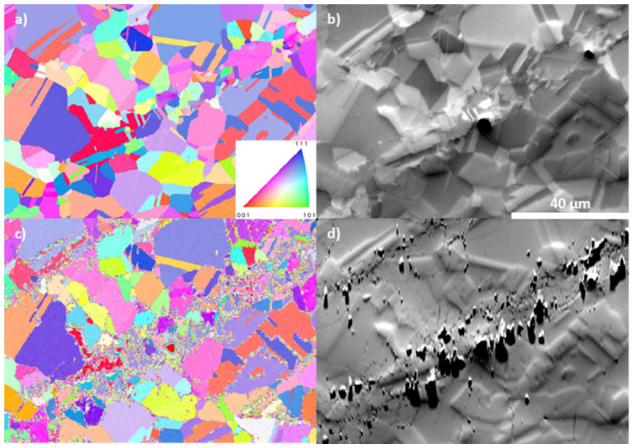

Fig. 3 IL-EBSD and IL-SEM of polished IN625 before (a) and (b) and after OER activation (c) and (d).

in standard EBSD maps. As shown in Fig. S2 and S3b, conventional EBSD primarily records noise due to the formation of a NiFe (oxy)hydroxide layer. Notably, such films can block EBSD even at thicknesses of a few tens of nanometres, consistent with films observed in the literature.[5] Examining larger grains with different orientations in the refined EBSD map in Fig. 3 reveals no clear correlation with grain orientation. In contrast, regions containing smaller grains exhibit a noisy EBSD signal after OER activation, likely due to the formation of a thicker and more uneven NiFe (oxy)hydroxide layer. Furthermore, close inspection reveals that the noisiest EBSD signal is located at grain boundaries, likely caused by surface roughening from intergranular corrosion driven by Cr depletion and the formation of δ-phase (Ni_3Nb) precipitates, a phenomenon commonly observed in thermally treated Inconel alloys.[15] The most pronounced restructuring is thus observed on smaller grains, where the aspect ratio of boundary to surface is higher and the presence of local deformations and substructure (as revealed by Kernel Average Misorientation analysis, Fig. S4). This is confirmed with additional IL-EBSD analysis in Fig. S3. We note that in order to enable reliable EBSD and EDS mappings, beam-induced carbon contamination was removed using an effective argon cleaning procedure (see SI). This step is essential for Ni-based polycrystalline OER electrocatalysts.

To complement the IL-EBSD analysis, we also performed IL energy dispersive spectroscopy (EDS) mappings. Averaged EDS revealed a notable compositional shift after electrochemical treatment, with the Ni/Cr/Fe/Mo/Nb/O (at%) ratio changing from 60.9/22.9/6.6/5.8/3.3/0.5 to 51.0/15.1/6.8/3.9/2.3/20.9.

This surface oxidation change aligns with Pourbaix diagrams, where Ni and Fe are prone to oxidation, while Cr, Mo, and Nb preferentially dissolve under OER conditions. IL-EDS mappings (Fig. 4) further revealed the inhomogeneous surface behavior of IN625. Before electrochemical cycling, Ni, Fe, and Cr were uniformly distributed, while Nb and Mo were locally enriched due to the presence of carbide and δ-phases, which dissolved upon OER activation (see Mo and Nb signals in Fig. 4 and IL-SEM in Fig. S5). Notably, in Fig. 4, blue grains oriented near the (111) direction showed more pronounced Cr depletion

This journal is © The Royal Society of Chemistry 2025

Open Access Article. Published on 14 August 2025. Downloaded on 8/23/2025 4:20:50 PM.
This article is licensed under a Creative Commons Attribution 3.0 Unported Licence.

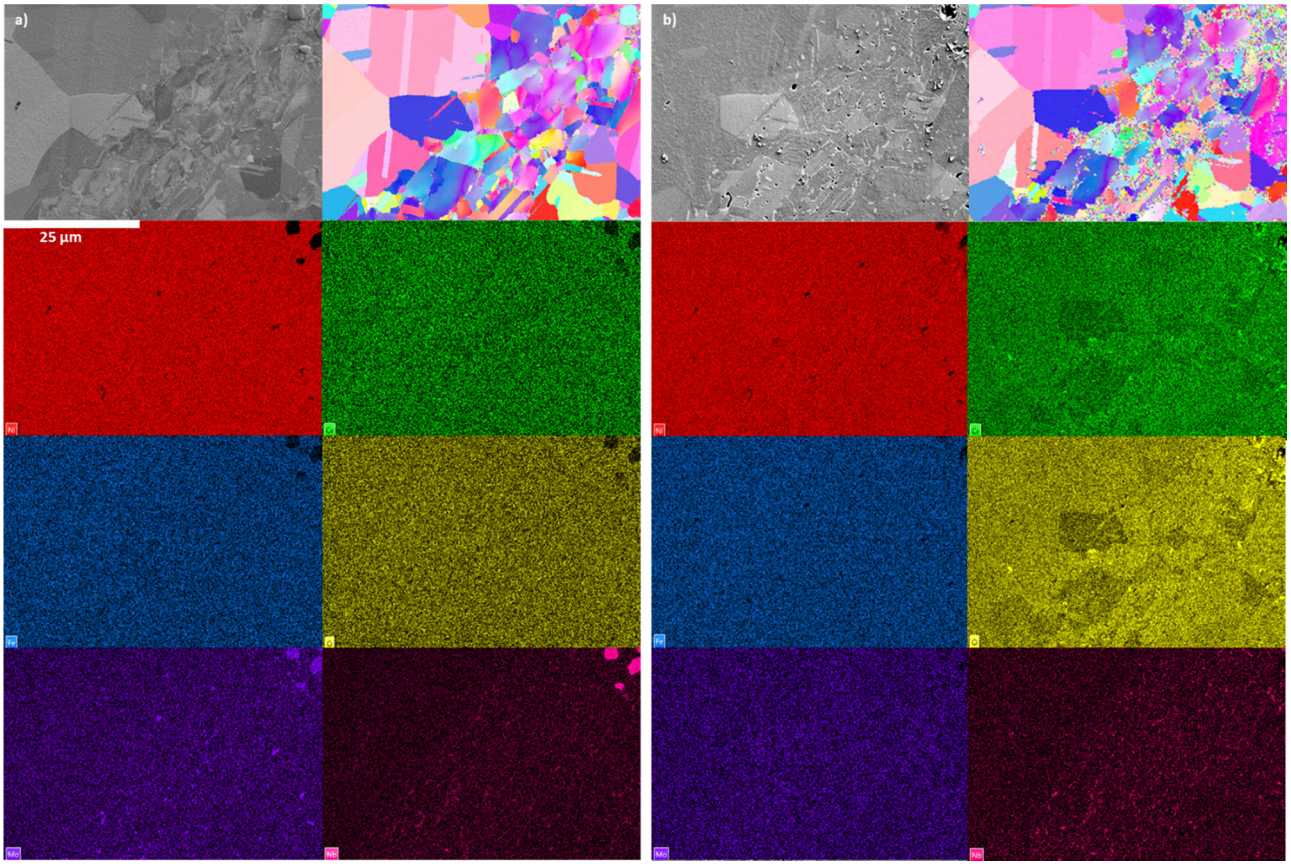

Fig. 4 IL-SEM, IL-EBSD IPF Z and IL-EDS maps of polished IN625: (a) before OER activation and (b) after OER activation. In IL-EDS mapping analysis, Ni locations and relative quantities are depicted with red, Cr in green, Fe in blue, O in yellow, Mo in violet and Nb in pink. (b) shows EBSD image from post-processing using spherical indexing.

and reduced surface oxidation, indicating a crystallographic influence on dissolution behavior that likely impacts subsequent OER film formation and performance.

To further validate the grain-dependent electrocatalytic behavior observed *via* IL-EBSD, we performed localized OER measurements using scanning electrochemical cell microscopy (SECCM). As shown in the final section of the SI, SECCM activity maps, recorded at ~5 µm lateral resolution, revealed up to 30% variation in OER activity across the surface, highlighting significant microscale heterogeneity. Correlating SECCM with EBSD showed that spots with grains oriented near the (111) direction and some with smaller grains in segregated regions exhibited higher OER activity. We must, however, note that deviations from these trends were also observed, suggesting that additional factors, such as the presence of different surface defects or even of δ-phases, can also influence electrocatalytic behavior. For further details, refer to the SI.

The integration of IL-EBSD with known IL-SEM and IL-EDS provides a robust framework and versatile toolbox for investigating local microstructural effects in complex, real-world materials, bridging metallurgical materials science and electrocatalysis. This grain-level perspective is particularly valuable for the development and post-processing of electrocatalytic alloys, where precise control over microstructure can lead to improved durability and activity.[17] Our methodology offers a blueprint for future studies on microstructure–activity–stability relationships and supports the rational design of electrocatalysts with tailored microstructures for renewable energy applications.

In summary, this study reveals the first direct correlation between grain-dependent microstructure and the formation of OER-active surface on a Ni-based superalloy using a newly developed IL-EBSD, complemented by IL-SEM and IL-EDS. We show that electrochemical activation under alkaline OER conditions leads to microstructure-dependent formation of different OER active sites, with (111)-oriented grains, smaller grains, and grain boundaries undergoing the most significant transformations. Specifically, (111) grains exhibit greater Cr depletion with reduced oxidation, while smaller grains, likely due to higher defect densities (*e.g.*, presence of strains and δ-phases), show increased surface roughening. SECCM measurements revealed up to 30% variation in local OER activity and partially confirmed enhanced performance for (111)-oriented and smaller grains; however, observed deviations from this trend indicate that additional microstructural and chemical factors also influence electrocatalytic behavior. These findings underscore the critical role of local microstructure in electrocatalyst behavior and establish IL-EBSD as a powerful tool for resolving crystallographic contributions to catalytic activity. Our findings demonstrate the untapped potential of combining classical metallurgical tools with electrochemical insight and offer a new

Open Access Article. Published on 14 August 2025. Downloaded on 8/23/2025 4:20:50 PM.
This article is licensed under a Creative Commons Attribution 3.0 Unported Licence.

strategy for engineering high-performance anodes for the green hydrogen economy. Additionally, we address two practical challenges arising in such measurements: how to access grain information beneath relatively thick surface films and how to effectively eliminate unwanted carbon deposition during SEM imaging.

The authors acknowledge ARIS research programs P2-0132, P2-0393, I0-0003 and I0-0006; projects N2-0248, N2-0337, J7-4636 and J7-50227; and NATO SPS grant G6230. A. V and J. U. acknowledge funding from the Belgian Walloon Region's TiNTHyN project.

Conflicts of interest

There are no conflicts to declare.

Data availability

The data supporting this article are included as part of the SI. Supplementary information available: Experimental details and additional EDS, EBSD and SECCM results. See DOI: **https://doi.org/10.1039/d5cc02703a**

References

1 R. Zhang, A. Xie, L. Cheng, Z. Bai, Y. Tang and P. Wan, *Chem. Commun.*, 2023, **59**, 8205–8221.
2 G. Wang, H. Li, F. Babbe, A. Tricker, E. J. Crumlin, J. Yano, R. Mukundan and X. Peng, *Adv. Energy Mater.*, 2025, 2500886.
3 M. W. Louie and A. T. Bell, *J. Am. Chem. Soc.*, 2013, **135**, 12329–12337.
4 F. Dionigi and P. Strasser, *Adv. Energy Mater.*, 2016, **6**, 1600621.
5 L. Magnier, G. Cossard, V. Martin, C. Pascal, V. Roche, E. Sibert, I. Shchedrina, R. Bousquet, V. Parry and M. Chatenet, *Nat. Mater.*, 2024, **23**, 252–261.
6 M. Etzi Coller Pascuzzi, A. J. W. Man, A. Goryachev, J. P. Hofmann and E. J. M. Hensen, *Catal. Sci. Technol.*, 2020, **10**, 5593–5601.
7 D. Friebel, M. W. Louie, M. Bajdich, K. E. Sanwald, Y. Cai, A. M. Wise, M.-J. Cheng, D. Sokaras, T.-C. Weng, R. Alonso-Mori, R. C. Davis, J. R. Bargar, J. K. Nørskov, A. Nilsson and A. T. Bell, *J. Am. Chem. Soc.*, 2015, **137**, 1305–1313.
8 D. Y. Chung, P. P. Lopes, P. Farinazzo, B. D. Martins, H. He, T. Kawaguchi, P. Zapol, H. You, D. Tripkovic, D. Strmcnik, Y. Zhu, S. Seifert, S. Lee, V. R. Stamenkovic and N. M. Markovic, *Nat. Energy*, 2020, **5**, 222–230.
9 A. Abdel Haleem, J. Huyan, K. Nagasawa, Y. Kuroda, Y. Nishiki, A. Kato, T. Nakai, T. Araki and S. Mitsushima, *J. Power Sources*, 2022, **535**, 231454.
10 Z. W. Seh, J. Kibsgaard, C. F. Dickens, I. Chorkendorff, J. K. Nørskov and T. F. Jaramillo, *Science*, 2017, **355**, eaad4998.
11 D. Raabe, J. R. Mianroodi and J. Neugebauer, *Nat. Comput. Sci.*, 2023, **3**, 198–209.
12 K. J. J. Mayrhofer, J. C. Meier, S. J. Ashton, G. K. H. Wiberg, F. Kraus, M. Hanzlik and M. Arenz, *Electrochem. Commun.*, 2008, **10**, 1144–1147.
13 N. Hodnik, M. Zorko, M. Bele, S. Hočevar and M. Gaberšček, *J. Phys. Chem. C*, 2012, **116**, 21326–21333.
14 B. Vanrenterghem, N. Hodnik, M. Bele, M. Šala, G. Amelinckx, S. Neukermans, R. Zaplotnik, G. Primc, M. Mozetič and T. Breugelmans, *Chem. Commun.*, 2017, **53**, 9340–9343.
15 L. Xu, J. Zhang, Y. Han, L. Zhao and H. Jing, *Corros. Sci.*, 2019, **160**, 108169.
16 W. C. Lenthe, L. Germain, M. R. Chini, N. Gey and M. De Graef, *Acta Mater.*, 2020, **188**, 579–590.
17 X. Xu, Y. Zhong, M. Wajrak, T. Bhatelia, S. P. Jiang and Z. Shao, *InfoMat*, 2024, **6**, e12608.

 This journal is © The Royal Society of Chemistry 2025